Fabrication of the high-Q Si$_3$N$_4$ microresonators for soliton microcombs

Shuai Wan (万 帅)[1,2], Rui Niu (牛 睿)[1,2], Jin-Lan Peng (彭金兰)[3], Jin Li (李 锦)[1,2], Guang-Can Guo (郭光灿)[1,2], Chang-Ling Zou (邹长铃)[1,2], and Chun-Hua Dong (董春华)[1,2*]

[1] CAS Key Laboratory of Quantum Information, University of Science and Technology of China, Hefei 230026, China

[2] CAS Center For Excellence in Quantum Information and Quantum Physics, University of Science and Technology of China, Hefei 230026, China

[3] Center for Micro and Nanoscale Research and Fabrication, University of Science and Technology of China, Chinese Academy of Sciences, Hefei 230026, China

*Corresponding author: chunhua@ustc.edu.cn

Received November 18, 2021 | Accepted December 13, 2021 | Posted Online January 5, 2022

The microresonator-based soliton microcomb has shown a promising future in many applications. In this work, we report the fabrication of high quality (Q) Si$_3$N$_4$ microring resonators for soliton microcomb generation. By developing the fabrication process with crack isolation trenches and annealing, we can deposit thick stoichiometric Si$_3$N$_4$ film of 800 nm without cracks in the central area. The highest intrinsic Q of the Si$_3$N$_4$ microring obtained in our experiments is about 6×10^6, corresponding to a propagation loss as low as 0.058 dBm/cm. With such a high Q film, we fabricate microrings with the anomalous dispersion and demonstrate the generation of soliton microcombs with 100 mW on-chip pump power, with an optical parametric oscillation threshold of only 13.4 mW. Our Si$_3$N$_4$ integrated chip provides an ideal platform for researches and applications of nonlinear photonics and integrated photonics.

Keywords: silicon nitride microresonator; optical frequency comb; dissipative Kerr soliton.

DOI: 10.3788/COL202220.032201

1. Introduction

The optical frequency comb, which is a series of equidistant coherent optical lines in the frequency domain, has been greatly developed in the past two decades[1–3]. The conventional optical frequency comb is produced by the mode-locked laser and has played an important role in the precise measurement of time and frequency[4–6]. Based on the optical field enhancement of the microresonator, in 2007, the generation of the optical frequency comb was realized in the microresonator by continuous-wave (CW) laser pumping[7], which opens a new field of optical frequency combs based on the microresonator. Due to the emergence of noise in the generation process[8], the early microresonator frequency combs showed low coherence, and their application value was not expected. In recent years, with the discovery of dissipative Kerr solitons[9], stable and fully coherent soliton microcombs can be obtained in microresonators by simultaneously balancing gain and loss, as well as dispersion and nonlinearity[10–13].

Compared with the conventional optical frequency comb generated by the mode-locked laser, the performance of the soliton microcomb has the advantages of low-power consumption, small footprint, simple structure, and integrability[2,14]. Therefore, in

addition to providing an ideal platform for the study of nonlinear physics[15–17], the soliton microcomb has shown a promising future in many applications, such as optical frequency synthesizer[18], optical atomic clock[19], light detection and ranging (LiDAR)[20–23], low-noise microwave source[24–27], coherent optical communication[28,29], quantum key distribution[30], dual-comb spectroscopy[31–34], and optical coherence tomography[35,36].

In recent years, because of the possibility to achieve ultra-low linear and nonlinear optical losses and engineer the dispersion of waveguides and microresonators precisely[37,38], silicon nitride (Si$_3$N$_4$), which is one of the most commonly used materials in the CMOS process[39,40], has been a leading platform for frequency comb generation[2]. Up to now, the highest quality (Q) factor reported in the Si$_3$N$_4$-based microresonator is about 4.2×10^8[41]. However, in order to reduce the optical loss, the thickness of such a microresonator is as low as 45 nm, and a large portion of the mode light fields is in the surrounding silicon oxide medium, resulting in dispersion that does not meet the requirements of the generation of soliton microcombs[8]. Recently, a novel fabrication process named the Damascene reflow process has been developed, and a recorded Q in the order of 10^7 has been obtained in thick (~800 nm)

dispersion-engineered Si₃N₄ microring resonators[42,43]. Different from the conventional subtractive process[37], this additive process can significantly reduce the scattering loss of waveguides by smoothing the silica sidewalls through the high temperature reflow and polishing the top surface of Si₃N₄ waveguides through chemical mechanical polishing (CMP)[44].

In this work, we adopt the traditional subtractive process to fabricate dispersion-engineered microring resonators. By introducing the crack isolation trenches and performing the annealing process to reduce the tensile stress, we successfully deposit thick stoichiometric Si₃N₄ film without cracks in the central area. With our optimized processing technology, the intrinsic Q is demonstrated to be as high as 6×10^6, corresponding to a propagation loss as low as 0.058 dBm/cm. Furthermore, in our dispersion-engineered microring resonators with a cross section of 1.8 µm × 800 nm, we also obtain an intrinsic Q of about 3×10^6 with a free spectral range (FSR) of about 230 GHz, and the four-wave mixing (FWM) threshold of about 13.4 mW. In such a high Q microring, we have demonstrated the generation of soliton microcombs with on-chip pump power of about 100 mW.

2. Device Fabrication

To generate the Kerr soliton in the microresonator, anomalous group velocity dispersion (GVD) is required for permitting the phase and energy matching of the nonlinear optical interactions. The material GVD of Si₃N₄ is normal in the communication band, and therefore, the geometric dispersion has to be engineered by precisely tailoring the cross section of the waveguide to make the overall waveguide GVD anomalous. Figures 1(a) and 1(b) show the typical simulated dispersion trends with varied waveguide cross-section dimensions. The waveguide dispersion is computed based on COMSOL Multiphysics, and the material dispersion is included by expressing the refractive index in the Sellmeier equations[45]. Here, the integrated dispersion D_{int} is adopted for the reason that D_{int} determines the spectrum width of the soliton microcomb and, compared to GVD, which needs to be anomalous at the pump resonance, a positive and relatively small D_{int} is necessary for the full span of the microcomb[8]. As shown in Fig. 1(a), D_{int} displays a monotonic increase with the increasing waveguide height and fixed width of 1.8 µm, and a waveguide height around 800 nm is required to reach the positive regime. In Fig. 1(b), with the variation of the waveguide width, zero points of the D_{int} can be shifted, which changes the width and the shape of the soliton microcomb.

From the above simulation results, for microcomb generation, the thickness of the Si₃N₄ device layer should be around 800 nm. Our fabrication process starts from the preparation of high Q Si₃N₄ film to match the anomalous dispersion. The original 4 in. (1 in. = 2.54 cm) substrate is made up of 500 µm silicon and 4 µm wet oxidation silicon dioxide (SiO₂). Since low losses are very important for nonlinear optics, we use low-pressure chemical vapor deposition (LPCVD) combined with post-annealing to deposit stoichiometric Si₃N₄ film with minimal absorption loss. However, due to the high tensile stress, the
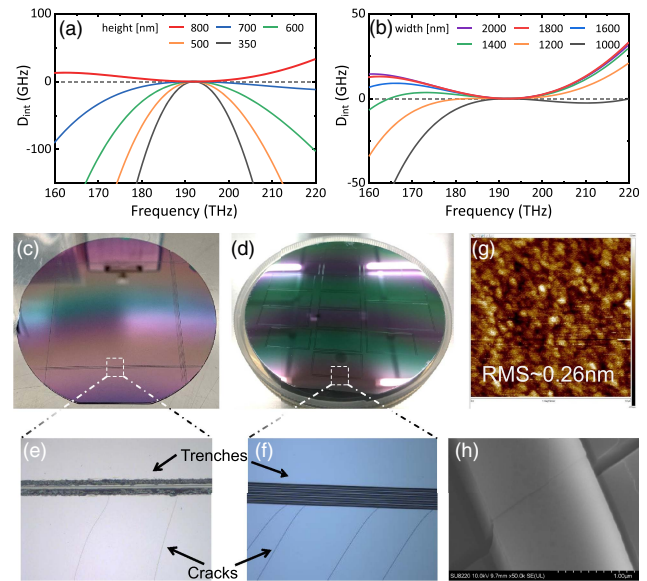

Fig. 1. (a) Simulated dispersion curves for different heights of the Si₃N₄ waveguide, with the waveguide width fixed at 1.8 µm. (b) Simulated dispersion curves for different widths of the Si₃N₄ waveguide, with the waveguide height fixed at 800 nm. (c) Using a diamond scriber on the 4 in. wafer to draw a square area. (d) Using lithography to define the patterns of the trenches. (e), (f) The relevant partial magnifications show that the cracks are successfully blocked by the trenches. (g) The surface range of 1 µm × 1 µm is scanned by atomic force microscopy (AFM), and the corresponding root-mean-square (RMS) roughness is 0.26 nm. (h) Scanning electron microscope (SEM) image of a crack passing through the etched waveguide.

stoichiometric Si₃N₄ film with thickness exceeding 400 nm easily cracks, as shown in Figs. 1(c)–1(f). These cracks typically start from the edge of the wafer and propagate into the central area[46]. Figure 1(h) shows the scanning electron microscope (SEM) image of a crack propagating through the etched waveguide. Such cracks can break the waveguides, seriously affecting the transmission of incident light. Therefore, in order to prevent film cracking, before Si₃N₄ deposition, defining crack isolation trenches is necessary and effective[46,47]. As proposed in Ref. [48], a staircase profile is needed to stop the cracking; here we implement two methods to define the trenches. One method is using a diamond scribe to create some trenches around the wafer, as shown in Fig. 1(e). Figure 1(f) shows another method, which uses lithography to define the patterns of trenches and then applies a buffered oxide etch (BOE) to etch through SiO₂ and thus to form 4 µm deep trenches. Then, the 800 nm Si₃N₄ film is deposited by LPCVD at 775°C in steps of approximately 400 nm thickness. Each step is followed by post-annealing at 1100°C in nitrogen atmosphere for 5 h to reduce the absorption loss and release the tensile stress. As the images show in Figs. 1(e) and 1(f), trenches made in both methods can effectively prevent the cracks. The corresponding root-mean-square (RMS) roughness of the deposited 800 nm film is 0.26 nm, as shown in Fig. 1(g).

The subtractive fabrication flow is illustrated in Fig. 2. The device is patterned by e-beam lithography with hydrogen-silsesquioxane (HSQ) resist. Following the development of the
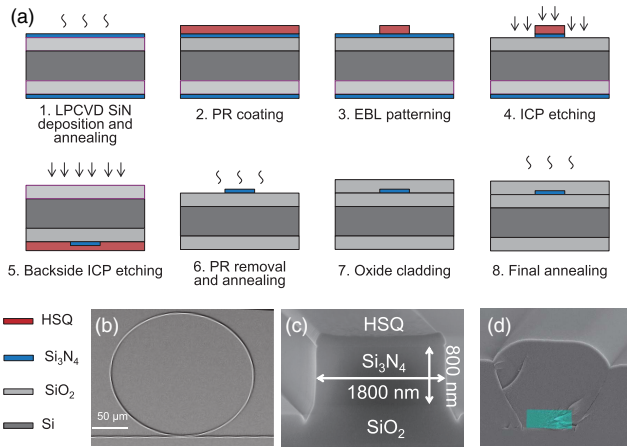
Fig. 2. (a) Fabrication process of the Si$_3$N$_4$ device. (b) SEM image of the Si$_3$N$_4$ microring resonator and bus waveguide. (c) SEM image of the cross-section view of the bus waveguide with photoresist, which is removed before SiO$_2$ depositing. The microtrench is at the bottom of each sidewall of the waveguide. (d) SEM image of the cross-section view of the bus waveguide after depositing the SiO$_2$ for protection. The Si$_3$N$_4$ waveguide is painted with green color.
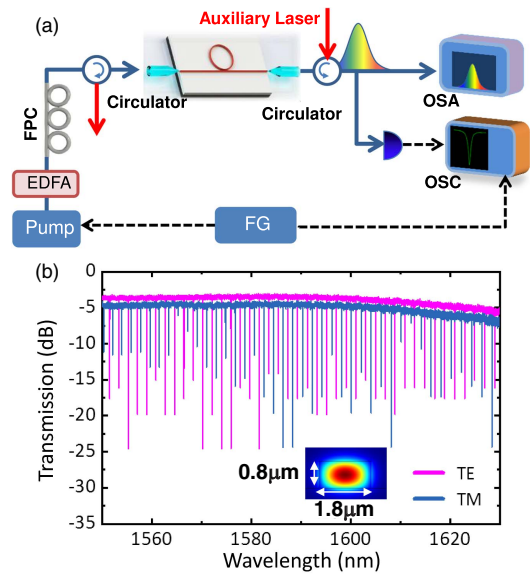

Fig. 3. (a) Schematic of the experimental setup. FPC, fiber polarization controller; EDFA, erbium-doped fiber amplifier; FG, function generator; OSA, optical spectrum analyzer; OSC, oscilloscope; PD, photon detector. (b) The typical transmission of fundamental TE (red curve) and TM (blue curve) modes from 1550 nm to 1630 nm. The envelope of the transmission line decreasing with the increase of wavelength is due to the power variation of the laser itself. Total insertion losses of fundamental TE modes and TM modes are about −3.6 dB and −4.5 dB, respectively.

pattern, the film is etched with a CHF$_3$/O$_2$-based gas in an inductively coupled plasma (ICP) etcher. Figure 2(b) shows the SEM image of the microring resonator after the etching process. As shown in Fig. 2(c), at the bottom of each sidewall of the waveguide, one microtrench is formed, which is also reported in Ref. [47]. We attribute this phenomenon to the formation of charged polymer SiF$_x$O$_y$ after the increase of the oxygen ratio[49], which attracts ions near the sidewall, increasing the rate of chemical reactions near the sidewall. These microtrenches, although no direct comparison has been made, may increase the scattering loss of the waveguide. After removing the residual resist with BOE, the Si$_3$N$_4$ film on the backside of the substrate is also etched to keep a balance of tensile stress between the front side and backside of the substrate. To further reduce the absorption loss, the substrate is again annealed at the aforementioned condition. Finally, an upper cladding of 3 μm SiO$_2$ is deposited by plasma-enhanced chemical vapor deposition (PECVD) to protect the sample, as shown in Fig. 2(d).

3. Optical Characterization of Microring

To realize soliton microcombs, we fabricate the microring resonator with a cross section of 1.8 μm × 800 nm according to the numerical prediction and a radius of 100 μm, as shown in Figs. 2(c) and 2(d). The bus waveguide has the same cross section as the microring to get a high coupling ideality[50]. To characterize the microring, a tunable CW laser (Toptica CTL 1550) is coupled into and out of the chip through lensed fibers, as indicated in Fig. 3(a). Figure 3(b) shows typical transmission spectra of fundamental TE (red curve) and TM (blue curve) modes from 1550 nm to 1630 nm with tens of microwatts pump power to avoid the thermal effect. The envelope of the

transmission line decreasing with the increase of wavelength is due to the power variation of the laser during wavelength sweeping. Because of the design and fabrication of inversed taper mode converters at facets of bus waveguides, the total insertion losses of fundamental TE modes and TM modes are as low as −3.6 dB and −4.5 dB, respectively.

The loaded Q of all TM and TE resonances within the measurement spectrum (blue and red cross) are extracted and shown in Fig. 4(a), and the loaded Q of the microring resonator fabricated from the Si$_3$N$_4$ film without the annealing process at fabrication flow (green and purple triangle) are also illustrated for comparison. It is clear that loaded Q is approximately doubly increased with annealing process, which can not only release the tensile stress inside the Si$_3$N$_4$ film, but also remarkably reduce the absorption loss[46]. Figure 4(b) shows the typical TM optical mode with a linewidth of 128 MHz, corresponding to a loaded Q factor of 1.5×10^6. In our experiments, we found that the linewidth of the fundamental TE mode is about twice that of the fundamental TM mode, as illustrated in the inset histogram of Fig. 4(a). This can be attributed to the larger scattering loss of sidewalls of microrings relative to the upper and lower surface.

To explore the narrowest linewidth available with our current processing technology, we fabricate the microring resonator with the same radius and height, but with a larger ring width of 3 μm. Because of the relatively large ring width, scattering loss from etched sidewalls is reduced. As shown in Fig. 4(c), the linewidth of the optical mode at 1552.6 nm is about 65 MHz,
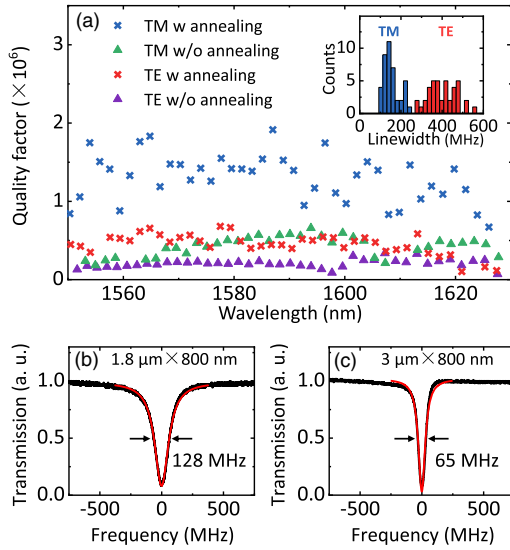
Fig. 4. (a) Loaded Q of the resonances in the microring with and without the annealing process of the Si$_3$N$_4$ film. The diameter of the microring is 200 μm with the cross section of 1.8 μm × 800 nm. The inset shows the histogram of the linewidth of fundamental TM (blue) and TE (red) modes. (b) The typical TM optical mode with the Lorentz fitting linewidth of about 128 MHz. (c) The typical transmission spectrum of the optical mode with the linewidth of 65 MHz in another microring with the cross section of 3 μm × 800 nm.

corresponding to a loaded Q_{load} factor of 3×10^6, and the intrinsic Q_{int} factor can be estimated as 6×10^6. The propagation loss is estimated as $\alpha = \nu_0/(Q_{int} \cdot R \cdot \mathrm{FSR}) = 0.058 \ \mathrm{dBm/cm}$[47], where ν_0 and R are the resonance frequency and the radius of the microring, respectively.

FWM is the basis of frequency comb generation, and the threshold is inversely proportional to squared Q. Therefore, the next step is to characterize the FWM threshold of our device, which has a cross section of 1.8 μm × 800 nm and a radius of 100 μm for optimized dispersion engineering. To obtain the threshold, a blue detuned laser is scanned to approach the resonance mode and stabilized at a blue detuning position, while the output light of the chip is measured by an optical spectrum analyzer (OSA). When the pump power exceeds the threshold, FWM can occur, which plays an important role in comb generation. As shown in Fig. 5, the output power of the primary FWM sidebands is recorded for different pump powers. The on-chip threshold power is $P_{th} \approx 13.4 \ \mathrm{mW}$ for a fundamental TM mode near 1562 nm with a loaded Q of about 1.5×10^6. The inset of Fig. 5 shows the optical spectrum with pump power $P = 13.9 \ \mathrm{mW}$, which is slightly above the threshold. It is obvious that the initial spacing of this primary comb state is not single but multiple FSRs, which is related to the mode linewidth and the dispersion of the device.

4. Soliton Microcombs

Further increasing the pump power and tuning the frequency of the pump laser, a series of frequency comb states and final
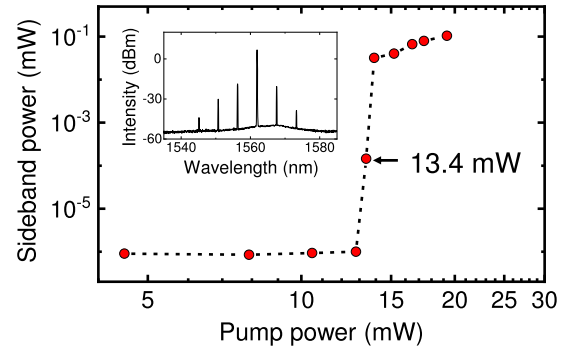

Fig. 5. Relationship between the output power of the primary FWM sidebands and the on-chip pump power of the microring resonator with a cross section of 1.8 μm × 800 nm and a radius of 100 μm, showing the FWM threshold of about 13.4 mW. Inset: optical spectrum with on-chip pump power of 13.9 mW.

soliton state can be generated from our device. To investigate the evolution of the comb states, the pump laser amplified by the erbium-doped fiber amplifier (EDFA) with an input power ~200 mW is launched to the chip. The on-chip pump power is about 100 mW. The microring resonator used in this experiment is the same as the above threshold measurement, and the pumped resonance mode is the fundamental TM mode around 1562.7 nm. For soliton comb generation, the pump laser needs to be scanned across the resonance mode from the blue side to the red side. However, because of the existence of the thermal effect[38,51,52], once the laser is scanned to the red side, the resonance frequency will experience a blue shift, making the soliton state unstable, as shown in Fig. 6(a). The evolution of the transmission with the primary comb state (Step 1), modulation instability oscillation state (Step 2), and soliton state (Step 3) is also clearly observed. More details are provided in our previous work[38].

To compensate the influence of the thermal effect in the high Q microring, as shown in Fig. 3(a), another auxiliary laser (red) is coupled to another optical mode in the opposite direction of pump laser[51,53]. Firstly, the pump and auxiliary lasers are settled at the blue detuning side of the cavity mode. When the auxiliary laser drops out of the cavity mode, the cavity cools down rapidly, and the resonance mode blue shifts, effectively scanning the pump to reach the dissipative Kerr soliton (DKS) state, as shown in Fig. 6(b). Then, the pump laser can easily stop at the soliton state and stably generate the soliton microcombs. Figures 6(c) and 6(d) show the optical spectra of multi-soliton and single soliton states when the pump laser stopped at different stages, corresponding to the different detunings. The single soliton state can be repeatedly reached by manually sweeping the laser to the soliton stage, and the smooth envelope of the single soliton state can be fitted by sech^2 function [red curve in Fig. 6(d)]. Several obvious distortions on the envelope are caused by avoided mode crossings[54,55].

5. Conclusion

In conclusion, we have presented the fabrication process of crack-free stoichiometric LPCVD Si$_3$N$_4$ film and ultra-low-loss
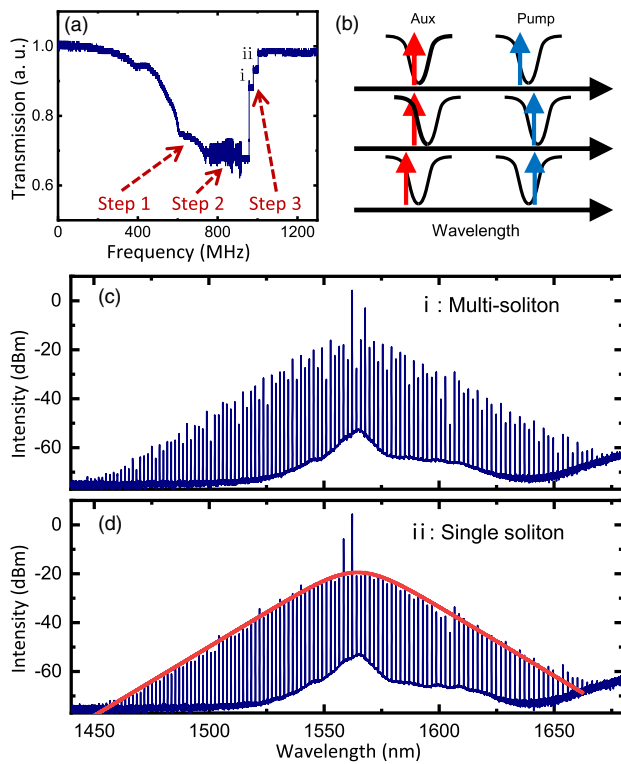
Fig. 6. (a) Evolution of the intracavity power as the laser frequency is scanning across the resonance mode. (b) Schematic of auxiliary-laser-assisted thermal response control method. The optical spectra of (c) multi-soliton and (d) single soliton states with the smooth envelope fitted by the sech^2 function (red curve).

Si_3N_4 waveguides and microring resonators. With the crack isolation trenches and the annealing process, cracks can be blocked out of the central area of the wafer. Based on the homemade LPCVD Si_3N_4 film, the highest intrinsic Q of about 6×10^6 has been observed in our fabricated microring resonator. Moreover, by designing the proper waveguide shape to engineer the dispersion, we have also demonstrated the FWM threshold of our device with $P_{th} \approx 13.4$ mW and the soliton microcomb generation with 100 mW on-chip pump power in the same device. Here, the Q factor could be further optimized, for example, by annealing the LPCVD Si_3N_4 film with a higher temperature to 1200°C[46,47] and reducing the surface roughness with CMP[44,56,57] or repetitive deposition after the etching[41]. On the other hand, the protected SiO_2 cladding can be deposited by the LPCVD, which owns the smaller absorption loss[46,47]. These processing technologies can further produce high Q and low insertion loss on-chip Si_3N_4 optical circuits, which are an ideal platform not only for the soliton microcomb, but also for nonlinear optics and integrated photonics.

Acknowledgement

References

1. T. J. Kippenberg, R. Holzwarth, and S. A. Diddams, "Microresonator-based optical frequency combs," Science **332**, 555 (2011).
2. T. J. Kippenberg, A. L. Gaeta, M. Lipson, and M. L. Gorodetsky, "Dissipative Kerr solitons in optical microresonators," Science **361**, eaan8083 (2018).
3. S. A. Diddams, K. Vahala, and T. Udem, "Optical frequency combs: coherently uniting the electromagnetic spectrum," Science **369**, eaay3676 (2020).
4. S. A. Diddams, D. J. Jones, J. Ye, S. T. Cundiff, J. L. Hall, J. K. Ranka, R. S. Windeler, R. Holzwarth, T. Udem, and T. W. Hänsch, "Direct link between microwave and optical frequencies with a 300 THz femtosecond laser comb," Phys. Rev. Lett. **84**, 5102 (2000).
5. D. J. Jones, S. A. Diddams, J. K. Ranka, A. Stentz, R. S. Windeler, J. L. Hall, and S. T. Cundiff, "Carrier-envelope phase control of femtosecond mode-locked lasers and direct optical frequency synthesis," Science **288**, 635 (2000).
6. T. Udem, R. Holzwarth, and T. W. Hänsch, "Optical frequency metrology," Nature **416**, 233 (2002).
7. P. Del'Haye, A. Schliesser, O. Arcizet, T. Wilken, R. Holzwarth, and T. J. Kippenberg, "Optical frequency comb generation from a monolithic microresonator," Nature **450**, 1214 (2007).
8. T. Herr, K. Hartinger, J. Riemensberger, C. Wang, E. Gavartin, R. Holzwarth, M. Gorodetsky, and T. Kippenberg, "Universal formation dynamics and noise of Kerr-frequency combs in microresonators," Nat. Photonics **6**, 480 (2012).
9. T. Herr, V. Brasch, J. D. Jost, C. Y. Wang, N. M. Kondratiev, M. L. Gorodetsky, and T. J. Kippenberg, "Temporal solitons in optical microresonators," Nat. Photonics **8**, 145 (2014).
10. H. Weng, J. Liu, A. Afridi, J. Li, J. Dai, X. Ma, Y. Zhang, Q. Lu, J. Donegan, and W. Guo, "Directly accessing octave-spanning dissipative Kerr soliton frequency combs in an AlN microresonator," Photonics Res. **9**, 1351 (2021).
11. X. Wang, P. Xie, W. Wang, Y. Wang, Z. Lu, L. Wang, S. Chu, B. Little, W. Zhao, and W. Zhang, "Program-controlled single soliton microcomb source," Photonics Res. **9**, 66 (2021).
12. Z. Lu, H.-J. Chen, W. Wang, L. Yao, Y. Wang, Y. Yu, B. E. Little, S. T. Chu, Q. Gong, W. Zhao, X. Yi, Y.-F. Xiao, and W. Zhang, "Synthesized soliton crystals," Nat. Commun. **12**, 3179 (2021).
13. W. Wang, L. Wang, and W. Zhang, "Advances in soliton microcomb generation," Adv. Photonics **2**, 034001 (2020).
14. B. Shen, L. Chang, J. Liu, H. Wang, Q.-F. Yang, C. Xiang, R. N. Wang, J. He, T. Liu, W. Xie, J. Guo, D. Kinghorn, L. Wu, Q.-X. Ji, T. J. Kippenberg, K. Vahala, and J. E. Bowers, "Integrated turnkey soliton microcombs," Nature **582**, 365 (2020).
15. H.-J. Chen, Q.-X. Ji, H. Wang, Q.-F. Yang, Q.-T. Cao, Q. Gong, X. Yi, and Y.-F. Xiao, "Chaos-assisted two-octave-spanning microcombs," Nat. Commun. **11**, 2336 (2020).
16. F. Shu, P. Zhang, Y. Qian, Z. Wang, S. Wan, C. Zou, G. Guo, and C. Dong, "A mechanically tuned Kerr comb in a dispersion-engineered silica microbubble resonator," Sci. China: Phys. Mech. Astron. **63**, 254211 (2020).
17. Q. Zhang, B. Liu, Q. Wen, J. Qin, Y. Geng, Q. Zhou, G. Deng, K. Qiu, and H. Zhou, "Low-noise amplification of dissipative Kerr soliton microcomb lines via optical injection locking lasers," Chin. Opt. Lett. **19**, 121401 (2021).
18. D. T. Spencer, T. Drake, T. C. Briles, J. Stone, L. C. Sinclair, C. Fredrick, Q. Li, D. Westly, B. R. Ilic, A. Bluestone, N. Volet, T. Komljenovic, L. Chang, S. H. Lee, D. Y. Oh, M.-G. Suh, K. Y. Yang, M. H. P. Pfeiffer, T. J. Kippenberg, E. Norberg, L. Theogarajan, K. Vahala, N. R. Newbury, K. Srinivasan, J. E. Bowers, S. A. Diddams, and S. B. Papp, "An optical-frequency synthesizer using integrated photonics," Nature **557**, 81 (2018).

19. Z. L. Newman, V. Maurice, T. Drake, J. R. Stone, T. C. Briles, D. T. Spencer, C. Fredrick, Q. Li, D. Westly, B. R. Ilic, B. Shen, M.-G. Suh, K. Y. Yang, C. Johnson, D. M. S. Johnson, L. Hollberg, K. J. Vahala, K. Srinivasan, S. A. Diddams, J. Kitching, S. B. Papp, and M. T. Hummon, "Architecture for the photonic integration of an optical atomic clock," Optica 6, 680 (2019).

20. M.-G. Suh and K. J. Vahala, "Soliton microcomb range measurement," Science 359, 884 (2018).

21. P. Trocha, M. Karpov, D. Ganin, M. H. P. Pfeiffer, A. Kordts, S. Wolf, J. Krockenberger, P. Marin-Palomo, C. Weimann, S. Randel, W. Freude, T. J. Kippenberg, and C. Koos, "Ultrafast optical ranging using microresonator soliton frequency combs," Science 359, 887 (2018).

22. J. Riemensberger, A. Lukashchuk, M. Karpov, W. Weng, E. Lucas, J. Liu, and T. J. Kippenberg, "Massively parallel coherent laser ranging using a soliton microcomb," Nature 581, 164 (2020).

23. J. Wang, Z. Lu, W. Wang, F. Zhang, J. Chen, Y. Wang, J. Zheng, S. Chu, W. Zhao, B. Little, X. Qu, and W. Zhang, "Long-distance ranging with high precision using a soliton microcomb," Photonics Res. 8, 1964 (2020).

24. W. Liang, D. Eliyahu, V. S. Ilchenko, A. A. Savchenkov, A. B. Matsko, D. Seidel, and L. Maleki, "High spectral purity Kerr frequency comb radio frequency photonic oscillator," Nat. Commun. 6, 7957 (2015).

25. W. Weng, E. Lucas, G. Lihachev, V. E. Lobanov, H. Guo, M. L. Gorodetsky, and T. J. Kippenberg, "Spectral purification of microwave signals with disciplined dissipative Kerr solitons," Phys. Rev. Lett. 122, 013902 (2019).

26. E. Lucas, P. Brochard, R. Bouchand, S. Schilt, T. Südmeyer, and T. J. Kippenberg, "Ultralow-noise photonic microwave synthesis using a soliton microcomb-based transfer oscillator," Nat. Commun. 11, 374 (2020).

27. J. Liu, E. Lucas, A. S. Raja, J. He, J. Riemensberger, R. N. Wang, M. Karpov, H. Guo, R. Bouchand, and T. J. Kippenberg, "Photonic microwave generation in the X- and K-band using integrated soliton microcombs," Nat. Photonics 14, 486 (2020).

28. P. Marin-Palomo, J. N. Kemal, M. Karpov, A. Kordts, J. Pfeifle, M. H. P. Pfeiffer, P. Trocha, S. Wolf, V. Brasch, M. H. Anderson, R. Rosenberger, K. Vijayan, W. Freude, T. J. Kippenberg, and C. Koos, "Microresonator-based solitons for massively parallel coherent optical communications," Nature 546, 274 (2017).

29. B. Corcoran, M. Tan, X. Xu, A. Boes, J. Wu, T. G. Nguyen, S. T. Chu, B. E. Little, R. Morandotti, A. Mitchell, and D. J. Moss, "Ultra-dense optical data transmission over standard fibre with a single chip source," Nat. Commun. 11, 2568 (2020).

30. F.-X. Wang, W. Wang, R. Niu, X. Wang, C.-L. Zou, C.-H. Dong, B. E. Little, S. T. Chu, H. Liu, P. Hao, S. Liu, S. Wang, Z.-Q. Yin, D.-Y. He, W. Zhang, W. Zhao, Z.-F. Han, G.-C. Guo, and W. Chen, "Quantum key distribution with on-chip dissipative Kerr soliton," Laser Photonics Rev. 14, 1900190 (2020).

31. M.-G. Suh, Q.-F. Yang, K. Y. Yang, X. Yi, and K. J. Vahala, "Microresonator soliton dual-comb spectroscopy," Science 354, 600 (2016).

32. A. Dutt, C. Joshi, X. Ji, J. Cardenas, Y. Okawachi, K. Luke, A. L. Gaeta, and M. Lipson, "On-chip dual-comb source for spectroscopy," Sci. Adv. 4, e1701858 (2018).

33. M. Yu, Y. Okawachi, A. G. Griffith, N. Picqué, M. Lipson, and A. L. Gaeta, "Silicon-chip-based mid-infrared dual-comb spectroscopy," Nat. Commun. 9, 1869 (2018).

34. Q.-F. Yang, B. Shen, H. Wang, M. Tran, Z. Zhang, K. Y. Yang, L. Wu, C. Bao, J. Bowers, A. Yariv, and K. Vahala, "Vernier spectrometer using counterpropagating soliton microcombs," Science 363, 965 (2019).

35. X. Ji, X. Yao, A. Klenner, Y. Gan, A. L. Gaeta, C. P. Hendon, and M. Lipson, "Chip-based frequency comb sources for optical coherence tomography," Opt. Express 27, 19896 (2019).

36. P. J. Marchand, J. Connor Skehan, J. Riemensberger, J.-J. Ho, M. H. P. Pfeiffer, J. Liu, C. Hauger, T. Lasser, and T. J. Kippenberg, "Soliton microcomb based spectral domain optical coherence tomography," Nat. Commun. 12, 427 (2021).

37. D. J. Moss, R. Morandotti, A. L. Gaeta, and M. Lipson, "New CMOS-compatible platforms based on silicon nitride and Hydex for nonlinear optics," Nat. Photonics 7, 597 (2013).

38. S. Wan, R. Niu, Z.-Y. Wang, J.-L. Peng, M. Li, J. Li, G.-C. Guo, C.-L. Zou, and C.-H. Dong, "Frequency stabilization and tuning of breathing soliton in Si_3N_4 microresonators," Photonics Res. 8, 1342 (2020).

39. A. Rahim, E. Ryckeboer, A. Z. Subramanian, S. Clemmen, B. Kuyken, A. Dhakal, A. Raza, A. Hermans, M. Muneeb, S. Dhoore, Y. Li, U. Dave, P. Bienstman, N. Le Thomas, G. Roelkens, D. Van Thourhout, P. Helin, S. Severi, X. Rottenberg, and R. Baets, "Expanding the silicon photonics portfolio with silicon nitride photonic integrated circuits," J. Lightw. Technol. 35, 639 (2017).

40. K. M. Latt, H. Park, H. Seng, T. Osipowicz, Y. Lee, and S. Li, "Effect of the silicon nitride passivation layer on the $Cu/Ta/SiO_2/Si$ multi-layer structure," Mater. Sci. Eng. B 90, 25 (2002).

41. M. W. Puckett, K. Liu, N. Chauhan, Q. Zhao, N. Jin, H. Cheng, J. Wu, R. O. Behunin, J. Wu, P. T. Rakich, K. D. Nelson, and D. J. Blumenthal, "422 million intrinsic quality factor planar integrated all-waveguide resonator with sub-MHz linewidth," Nat. Commun. 12, 934 (2021).

42. M. H. P. Pfeiffer, A. Kordts, V. Brasch, M. Zervas, M. Geiselmann, J. D. Jost, and T. J. Kippenberg, "Photonic damascene process for integrated high-Q microresonator based nonlinear photonics," Optica 3, 20 (2016).

43. M. H. P. Pfeiffer, J. Liu, A. S. Raja, T. Morais, B. Ghadiani, and T. J. Kippenberg, "Ultra-smooth silicon nitride waveguides based on the damascene reflow process: fabrication and loss origins," Optica 5, 884 (2018).

44. M. H. P. Pfeiffer, C. Herkommer, J. Liu, T. Morais, M. Zervas, M. Geiselmann, and T. J. Kippenberg, "Photonic Damascene process for low-loss, high-confinement silicon nitride waveguides," IEEE J. Sel. Top. Quantum Electron. 24, 6101411 (2018).

45. X. Zhang, G. Lin, T. Sun, Q. Song, G. Xiao, and H. Luo, "Dispersion engineering and measurement in crystalline microresonators using a fiber ring etalon," Photonics Res. 9, 2222 (2021).

46. K. Luke, A. Dutt, C. B. Poitras, and M. Lipson, "Overcoming Si_3N_4 film stress limitations for high quality factor ring resonators," Opt. Express 21, 22829 (2013).

47. Y. Xuan, Y. Liu, L. T. Varghese, A. J. Metcalf, X. Xue, P.-H. Wang, K. Han, J. A. Jaramillo-Villegas, A. Al Noman, C. Wang, S. Kim, M. Teng, Y. J. Lee, B. Niu, L. Fan, J. Wang, D. E. Leaird, A. M. Weiner, and M. Qi, "High-Q silicon nitride microresonators exhibiting low-power frequency comb initiation," Optica 3, 1171 (2016).

48. K. H. Nam, I. H. Park, and S. H. Ko, "Patterning by controlled cracking," Nature 485, 221 (2012).

49. B. Kim, J. Bae, and B. T. Lee, "Microtrench depth and width of SiON plasma etching," Vacuum 81, 338 (2006).

50. M. H. P. Pfeiffer, J. Liu, M. Geiselmann, and T. J. Kippenberg, "Coupling ideality of integrated planar high-Q microresonators," Phys. Rev. Appl. 7, 024026 (2017).

51. H. Zhou, Y. Geng, W. Cui, S.-W. Huang, Q. Zhou, K. Qiu, and C. W. Wong, "Soliton bursts and deterministic dissipative Kerr soliton generation in auxiliary-assisted microcavities," Light Sci. Appl. 8, 50 (2019).

52. X. Liu, X.-S. Yan, X. Zhang, Y. Liu, H. Li, Y. Chen, and X. Chen, "Tunable single-mode laser on thin film lithium niobate," Opt. Lett. 46, 5505 (2021).

53. Z. Lu, W. Wang, W. Zhang, S. T. Chu, B. E. Little, M. Liu, L. Wang, C.-L. Zou, C.-H. Dong, B. Zhao, and W. Zhao, "Deterministic generation and switching of dissipative Kerr soliton in a thermally controlled micro-resonator," AIP Adv. 9, 25314 (2019).

54. X. Yi, Q.-F. Yang, X. Zhang, K. Y. Yang, X. Li, and K. Vahala, "Single-mode dispersive waves and soliton microcomb dynamics," Nat. Commun. 8, 14869 (2017).

55. C. Bao, Y. Xuan, D. E. Leaird, S. Wabnitz, M. Qi, and A. M. Weiner, "Spatial mode-interaction induced single soliton generation in microresonators," Optica 4, 1011 (2017).

56. Z. Wang, C. Wu, Z. Fang, M. Wang, J. Lin, R. Wu, J. Zhang, J. Yu, M. Wu, W. Chu, T. Lu, G. Chen, and Y. Cheng, "High-quality-factor optical microresonators fabricated on lithium niobate thin film with an electro-optical tuning range spanning over one free spectral range," Chin. Opt. Lett. 19, 060002 (2021).

57. J. Lin, F. Bo, Y. Cheng, and J. Xu, "Advances in on-chip photonic devices based on lithium niobate on insulator," Photonics Res. 8, 1910 (2020).